

Emergence of a Helical Metal in Rippled Ultrathin Topological Insulator Sb_2Te_3 on Graphene

Francisco Muñoz* and Manuel Fuenzalida

Departamento de Física, Facultad de Ciencias, Universidad de Chile & CEDEENNA, Santiago, Chile

Paula Mellado

School of Engineering and Sciences, Universidad Adolfo Ibáñez, Santiago, Chile

Hari C. Manoharan

Department of Physics, Stanford University, Stanford, CA 94305, United States

Valentina Gallardo and Carolina Parra†

Departamento de Ingeniería Mecánica, Universidad Técnica Federico Santa María, Avenida España 1680, Valparaíso, Chile

The integration of topological insulators (TIs) with graphene offers a pathway to engineer hybrid quantum states, yet the impact of strain at the 2D limit remains a critical open question. Here, we investigate the structural properties of ultrathin (1 quintuple layer) Sb_2Te_3 grown on single-layer graphene and, motivated by the structural modulations observed at the TI surface, explore theoretically how such nanoscale corrugations may influence the electronic behavior of the system. Using low-temperature scanning tunneling microscopy (LT-STM), we observe a periodic rippling of the heterostructure with a wavelength of ~ 8.7 nm. Energetic analysis reveals that these ripples are not intrinsic but are driven by strain from the substrate during cooling. Density functional theory (DFT) calculations show that while the ideal flat heterostructure exhibits a hybridization gap of ~ 40 meV, the ripple-induced structural modulation closes this gap, restoring a metallic state. This gapless phase is not a trivial metal. By combining an effective moiré ladder model with spin-resolved DFT, we find that the proximity-induced spin-orbit coupling is redistributed across a dense manifold of minibands. The resulting “Helical Metal” has a complex spin-texture beyond a simple Rashba splitting. Remarkably, while the flat system is effectively spinless in this ultrathin limit due to hybridization, the ripples actively restore the spin polarization. Our findings suggest that rippled TI/graphene heterostructures provide an interesting platform to develop spintronics, where geometric modulation unlocks dense helical states that are inaccessible in the pristine flat limit.

I. INTRODUCTION

The integration of the topological insulator Sb_2Te_3 with graphene marks a significant advancement in the field of van der Waals heterostructures, which aim to engineer electronic properties through the controlled stacking of atomic layers [1–3]. The quintuple layer (QL) structure of Sb_2Te_3 , defined by its repeating unit of five atomic layers, serves as a precise template for constructing hybrid interfaces. This heterostructure enables the coupling of massless Dirac fermions in graphene with the helically spin-polarized surface states of the topological insulator, facilitating emergent phenomena inaccessible to either material alone [4]. The structural interplay at the interface can induce the formation of moiré superlattices [5–7] and periodic ripples. These features convert physical strain into a tunable parameter for manipulating quantum states. Consequently, the Sb_2Te_3 /graphene heterostructure emerges as a promising platform for next-generation spintronic and straintronic devices, where information is encoded not only in charge but also in spin

and valley degrees of freedom.

In Sec. II, we present the experimental realization of such a Sb_2Te_3 /graphene heterostructure, characterized by periodic ripples with a wavelength of ~ 8.7 nm. We offer an explanation for the physical origin of these ripples in Sec. III. In Sec. IV, we investigate, from a theoretical perspective, the electronic properties that such buckling is expected to induce using density functional theory and effective models. Finally, we draw the main conclusions.

II. 1QL Sb_2Te_3 NANOPLATELET GROWN ON SINGLE-LAYER GRAPHENE

Sb_2Te_3 is a tetradymite semiconductor that has been identified as a three-dimensional strong topological insulator (TI) and exhibits a rhombohedral crystal structure with the space group D_{3d}^5 or $R\bar{3}m$ [8]. This material has a layered structure, with each layer consisting of a triangular lattice of a single atomic species, either Sb or Te. Five such layers constitute one quintuple layer (QL) unit. Fig. 1a shows the structure of the material. Covalent bonding predominates within each QL, while the interaction between QLs is primarily van der Waals in nature. As a result, Sb_2Te_3 is typically manipulated in units of

* fvmunoz@gmail.com

† carolina.parra@usm.cl

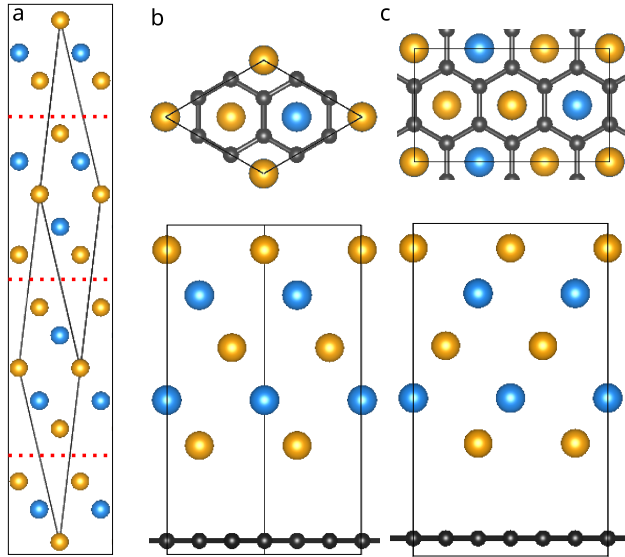


FIG. 1. (a) Crystal structure of Sb₂Te₃. The rhombohedral primitive cell is denoted by the inner black lines, and the quintuple layers are separated by dotted red lines. Each QL is nearly 1 nm wide. Along the article Te, Sb, C atoms are colored orange, cyan and black, respectively. (b) Top and lateral view of the primitive cell of 1 QL of Sb₂Te₃ on graphene (vacuum space is trimmed). (c) orthogonal cell of the heterostructure used to calculate buckling.

QLs, and the analysis here focuses on a few QLs.

TI/SLG nano-heterostructures based on thin Sb₂Te₃ nanplatelets (NPs) were grown on single-layer graphene (SLG). The TI synthesis parameters were tuned to obtain nanostructures thinner than 30 nm, *i.e.* below the 3D to 2D crossover limit[9], to promote the hybridization between top and bottom surface states, and their interaction with the SLG Dirac cone. Sb₂Te₃ NPs were synthesized by a catalyst-free vapor transport and deposition process. The resulting nano-heterostructures (Fig.2e) were characterized by low-temperature scanning tunneling microscopy LT-STM, to obtain information on their structural properties (see Appendix A 1 for additional details). We obtained lattice constant of $a_g = 2.456 \text{ \AA}$ for the graphene monolayer, and $a_{1QL} = 4.269 \text{ \AA}$ for a single quintuple layer (QL) of Sb₂Te₃. A $\sqrt{3} \times \sqrt{3}$ supercell of graphene (*e.g.* 6 atoms, a full hexagon) has a lattice constant of 4.254 \AA , with just 0.35% of mismatch with the Sb₂Te₃ monolayer, see Fig. 1b-c.

Fig.2a shows a buckling pattern observed on the surface of a 1QL Sb₂Te₃ NP grown on single-layer graphene. The angle-dependent spatial correlation function $\langle G_\theta(r) \rangle$ (Fig.2b) was calculated for the topographic image shown in Fig.2a. $\langle G_\theta(r) \rangle$ reflects the spatial pattern observed in the topographic image, which shows a particular spatial pattern with a characteristic length scale [10]. In Fig.2b, arcs of intensity that repeat with a fixed periodicity are marked; these imply a pattern of phase separation of low and high topographic regions over large length scales. These intensity arcs are consistent with the real-space

phase separation of a topographic striped pattern. The functional form of these arcs for a system with stripes separated by a distance $d \approx 8.7 \text{ nm}$ and running along an angle α from the horizontal, measured at an angle θ , is $Nd/\cos((\alpha-90)-\theta)$.

Due to thermal cycling, buckling of graphene can be triggered by compressive strain [11]. Under such strain, graphene buckles out of plane, forming wrinkles, ripples, or bubbles. Fig.2c and Fig.2d show STM topographies of the ripples found in the SLG transferred onto SiO₂, after post-growth thermal treatment. The nano-heterostructure sample presented here undergoes a thermal treatment before LT-STM measurements as well. The TI nanplatelet grown on this strained graphene substrate leads to spatial height modulation, forming corrugated ripples, as seen in Fig.2a. Although the height modulation of the observed buckling pattern in the NP is around 0.6 nm, the mean surface roughness is around 0.18 nm, a value similar to the one found in buckled graphenesuperlattices [12].

III. ORIGIN OF THE RIPPLES IN SAMPLES

To determine the physical origin of the observed ripples, we first evaluated whether the corrugation arises from an intrinsic instability of the freestanding Sb₂Te₃/graphene heterostructure or from the formation of distinct material phases. Our energetic analysis (detailed in Appendix A 3) yields three key findings. First, the van der Waals binding energy between the layers ($E_{bind} \approx 0.23 \text{ eV/cell}$) is significantly larger than the estimated bending energy of the rippled stack (estimation of an upper bound, $E_{bend} \approx 0.20 \text{ eV/stripe}$), ensuring that the two materials remain coupled rather than delaminating. Second, the energy penalties for relative sliding and intrinsic strain accumulation are negligible ($< 0.01 \text{ eV}$), ruling out stress-induced buckling from lattice mismatch. Third, the formation of alternating Sb_xTe_{1-x} phases is energetically unfavorable due to high phase-boundary costs. Furthermore, molecular dynamics simulations of the freestanding system show no spontaneous stripe formation. Consequently, the ripples cannot be intrinsic to the heterostructure itself and must be driven by external factors.

Having ruled out intrinsic mechanisms, we conclude that the observed ripples originate from a pre-existing buckled structure in the graphene substrate. The formation of this structure can be understood as a two-step process: substrate preparation followed by growth. First, during the wet transfer process, the graphene film is deposited from solution onto the SiO₂ substrate. As the meniscus drains, directional capillary forces can create an initial, anisotropic set of wrinkles aligned along a preferential axis [13], imposing a one-dimensional structural template on the graphene before any additional processing. Next, the Graphene/SiO₂ substrate is heated for Sb₂Te₃ growth and subsequently cooled. Due to

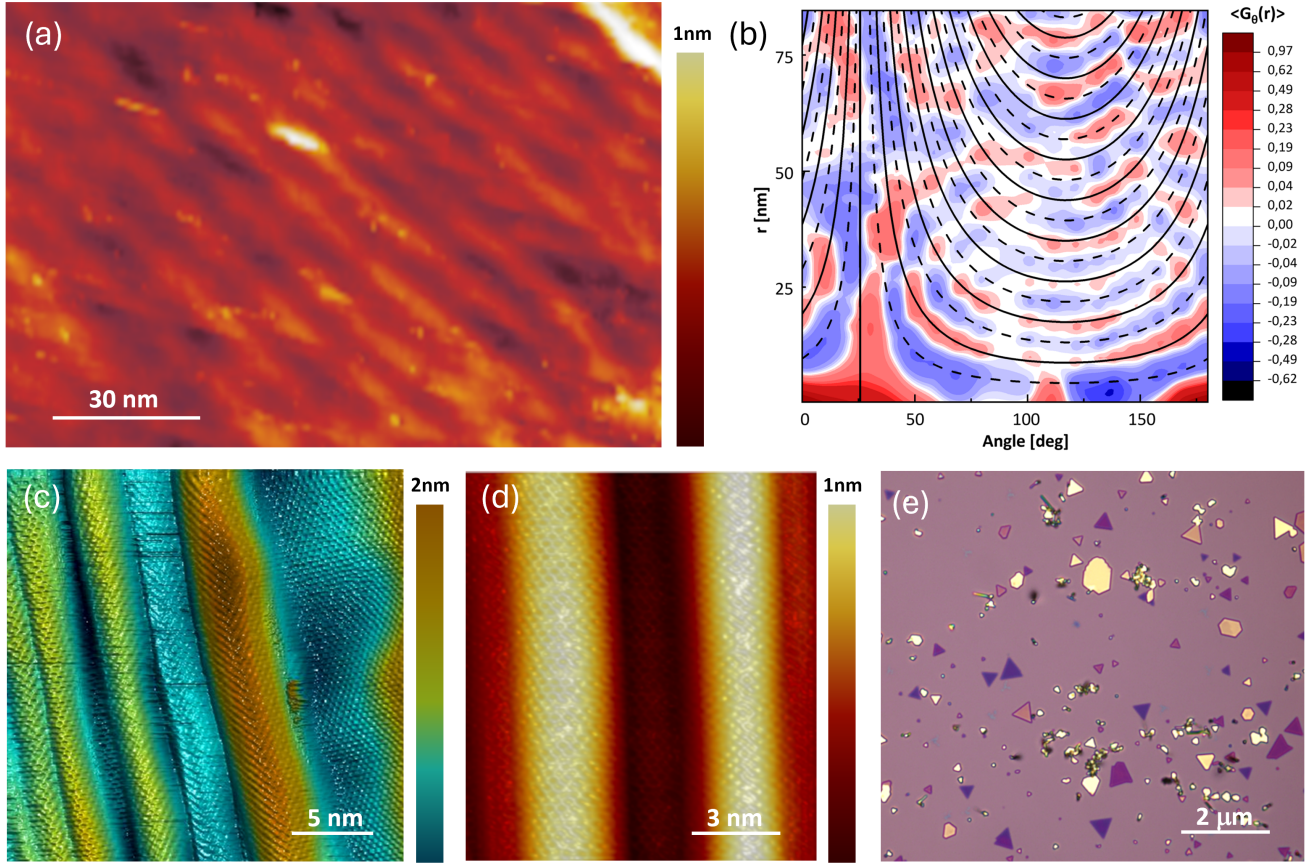


FIG. 2. (a) STM topography of the modulated pattern found in the surface of a 1QL Sb₂Te₃ nanplatelet grown on single-layer graphene. (b) Angle-dependent correlation function for the stripes in (a). The color scale on the right-hand side plots represents the value of $\langle G_\theta(r) \rangle$. This quantity is plotted as a function of $|r|$ (vertical axis) and the angle θ with the horizontal axis. The angle-dependent correlation functions reveal clear arcs of intensity, associated with the stripe-like modulation on the surface of Sb₂Te₃ nanplatelet. Solid and dashed lines represent the best fits to $Nd/\cos[(\alpha-90^\circ)-\theta]$ and $(2N-1)w/\cos[(\alpha-90^\circ)-\theta]$ for the local maxima and minima, respectively, as described in the main text. (c) and (d) STM topography of uniaxial ripples found in CVD SLG transfer onto SiO₂, after the cooling-down process. (e) Optical microscope image of Sb₂Te₃ nanplatelets grown on graphene/SiO₂ where optical contrast shows nanplatelets are in the range of a few quintuple layers (light purple) up to several QLs (yellowish) thick

the mismatch in thermal expansion coefficients between graphene and SiO₂ [11], significant thermal strain develops. Because the graphene has a negative thermal expansion coefficient (expanding upon cooling) while the substrate contracts, the sheet experiences compressive strain. To relieve this, the graphene buckles along the previously formed wrinkles, which serve as lines of weakness, amplifying a highly periodic ripple pattern. The Sb₂Te₃ monolayer grows conformally over this pre-rippled graphene template. This model also explains why the effect is not observed for thicker films: as energetic considerations suggest, the bending energy of a stack thicker than 1QL would be too high for the available thermal strain energy to overcome, making buckling energetically unfavorable.

IV. ELECTRONIC STRUCTURE: DENSITY FUNCTIONAL THEORY RESULTS

A. Electronic Properties of the heterostructure without ripples

The defining feature of Moiré superstructures is their potential to host exotic electronic states. To isolate the theoretical electronic effects that ripples of the type observed experimentally could induce, we first establish a theoretical baseline by calculating the electronic structure of an ideal, flat Sb₂Te₃/graphene heterostructure using DFT (see Appendix for details). This reference system consists of a 1×1 unit cell of Sb₂Te₃ on a $\sqrt{3} \times \sqrt{3}$ graphene supercell, with a minimal lattice mismatch of 0.35% (see Fig. 1b). In its bulk form, Sb₂Te₃ is a well-known 3D TI, characterized by a metallic surface

state protected within its bulk band gap of $E_{gap} \sim 0.19$ eV [8, 14].

Figure 3 (top panel) shows the band structure of a freestanding single QL (*i.e.* without graphene). It reveals a small but finite gap (0.45 eV) arising from the interaction between the upper and lower surface states. This gap signifies the loss of topological character in the ultrathin limit, caused by wavefunction overlap between the slab's surfaces. The resulting hybridization opens a gap at the Dirac point, triggering a topological phase transition. Such quantum-confinement effects are well documented in thin-film TIs; for instance, the related Bi_2Se_3 is experimentally confirmed to become fully insulating below six QLs [9]. For comparison, excluding spin-orbit coupling (SOC) yields a larger trivial gap of 0.73 eV.

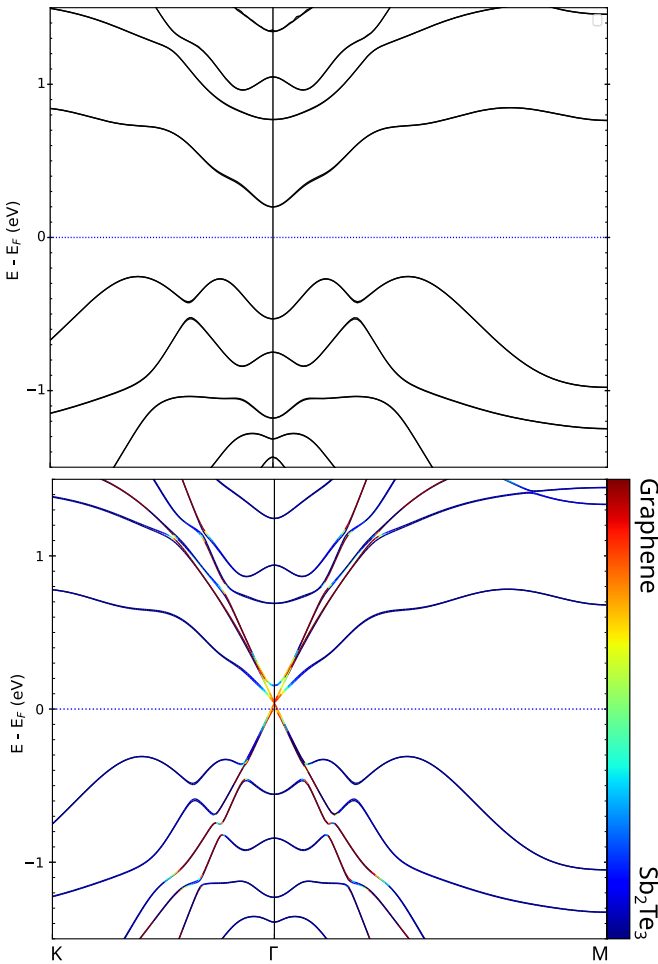


FIG. 3. Band structure of a single QL of Sb_2Te_3 : freestanding (top) and on graphene (bottom). SOC is included. The Dirac cone from graphene is folded to Γ . At this energy scale, the bands appear spin-degenerate; the Rashba spin texture becomes visible only at much higher magnification.

When the Sb_2Te_3 thin film is placed on graphene (Fig. 3, bottom panel), there is a strong hybridization of the bands at Γ , right at the Fermi level. This is a

direct consequence of the $\sqrt{3} \times \sqrt{3}$ reconstruction, which folds the graphene K and K' valleys to the zone center. At Γ , the graphene contributes eight bands (2 valleys \times 2 spins \times 2 branches) that become nearly degenerate with the Sb_2Te_3 states.

A zoom into the band structure reveals that this interaction lifts the degeneracy, splitting the bands into two massive Dirac cones with gaps of 10 and 40 meV. This behavior can be understood as a *Dirac-Dirac resonance*: the folding forces the graphene and TI Dirac cones to align in both momentum (Γ) and energy. The resulting hybridization is strong enough to open a global gap in the heterostructure, effectively rendering the TI surface states sensitive to the graphene layer—a surprising deviation from the behavior of thicker TI films, where the surface states typically remain robust. These results agree with earlier calculations [15] and measurements [16]. In other typical TI materials, a larger mismatch shifts both Dirac cones in energy, avoiding this resonance [2, 17].

For the sake of comparison, if SOC is not included, there is no such strong hybridization at Γ ; the bands resemble the top panel of Fig. 3 with the graphene Dirac cone superimposed, along with minor avoided crossings.

In thicker Sb_2Te_3 samples on graphene, this strong Dirac-Dirac resonance is diminished. As the top and bottom surface states decouple, only the bottom surface state physically interacts with the substrate. Consequently, there is only one degenerate Kramers pair at Γ available to interact with the graphene's folded Dirac cones (which constitute two Kramers pairs), leading to a fundamentally different and less effective hybridization landscape [18, 19].

B. Electronic properties of the heterostructure with ripples

To characterize the electronic influence of the buckling, we modeled the simplest periodic ripple case, excluding secondary effects such as shear stress. For this purpose, we employed the orthogonal supercell shown in Fig. 4a. Its short axis corresponds to the pristine unit cell width, while the long axis is repeated to match the experimentally observed ripple wavelength. Although not presented here, calculations for six other wavelengths yielded qualitatively similar results. In the structural relaxation, the out-of-plane (z) positions of the graphene atoms were fixed to the cosine profile, while all other degrees of freedom were allowed to relax. The supercell lattice vector along the ripple direction was shortened to conserve the total arc length of the graphene sheet relative to its flat state, thereby mimicking the physical relaxation of compressive strain (see Appendix for details).

The resulting electronic structure is shown in Fig. 4b. On a large energy scale, it resembles the flat unit cell but folded into the smaller mini-Brillouin zone defined by the long-period superlattice. However, the low-energy physics (Fig. 4c) reveals two striking phenomena distinct

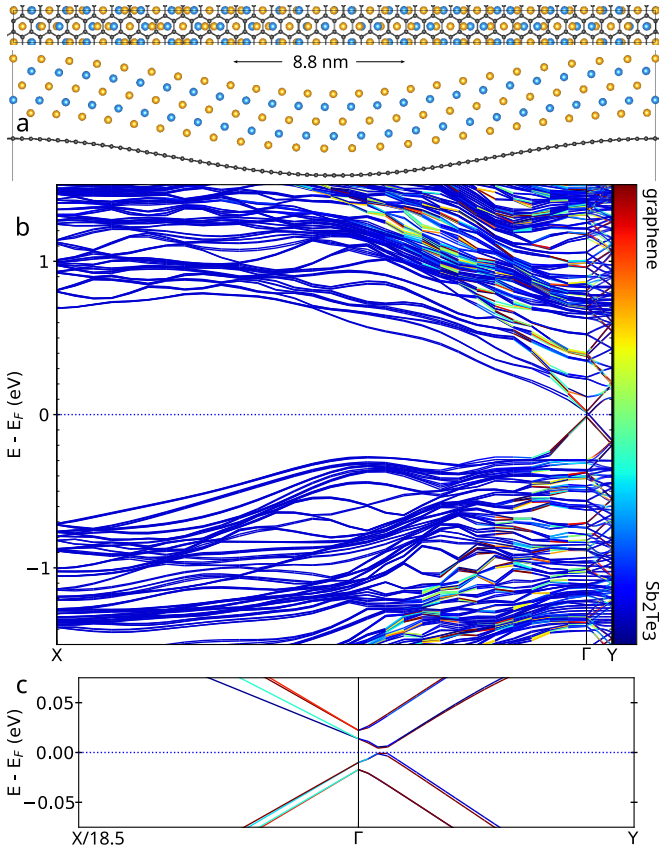


FIG. 4. (a) Top and lateral views of the supercell used to model the electronic structure of the ripples. (b) Band structure of the rippled supercell; X and Y correspond to directions perpendicular to and along the ripples, respectively. (c) Zoom of the low-energy bands near the Fermi level.

from the flat case: (i) the Dirac cone is shifted away from the high-symmetry Γ point, and (ii) this shifted Dirac cone becomes effectively gapless (< 1 meV).

For a bare graphene layer, a momentum shift of the Dirac cone is expected. The local lattice deformation (compression and elongation) induced by buckling creates a pseudo-vector potential \mathbf{A} that acts as a gauge field, shifting the Dirac point from \mathbf{K} to $\mathbf{K} - \mathbf{A}$ without opening a gap [20] (note that \mathbf{K} is folded to Γ in the supercell). Although the varying strain field can theoretically induce a pseudo-Landau level structure, such quantization is not observed here, likely because the strain magnitude is too small or due to hybridization effects. Crucially, unlike the bare case, the graphene cone here remains hybridized with the Sb_2Te_3 surface states. The fact that the gap closes (restoring metallicity) suggests that the symmetry breaking induced by the ripple disrupts the specific hybridization conditions that opened the ~ 40 meV gap in the flat heterostructure.

It is important to note that this buckling mechanism fundamentally differs from electronic instabilities like Charge Density Waves (CDW). In a CDW, a lattice distortion occurs spontaneously to lower the total

electronic energy by opening a gap at the Fermi level. In our case, the buckling increases the elastic energy of the Sb_2Te_3 layer without a compensating electronic gain. Quite the opposite: our DFT calculations show that the system transitions from a gapped (flat) state to a gapless (rippled) state, increasing the population of states at the Fermi level. This confirms that the ripples are driven not by electronic energy minimization, but by the extrinsic release of thermal strain from the substrate.

C. Emergence of a Helical Metal

The transition to a gapless state in the presence of ripples raises a fundamental question about the topological character of the quasiparticles. In the flat heterostructure, hybridization opens a gap, effectively destroying the single Dirac cone. One might expect that the additional disorder from the ripples would result in a trivial metallic state without a clear spin character. To understand the interplay between the ripples, acting as a moiré modulation, and the spin-orbit coupling, we developed an effective ladder model (detailed derivation and formalism in Appendix A 4). The model reveals that while the ripples modifies the simple band structure, it promotes a spin-momentum locking. Instead of a clean Rashba splitting, the moiré potential generates a dense manifold of minibands (see Appendix Fig. 7), where the helicity is distributed across the entire low-energy spectrum. This suggests that the system behaves as a “Helical Metal”: a state where the density of states at the Fermi level is composed entirely of states with strong spin-momentum locking. Helical states have been observed in moiré heterostructures featuring proximity induced SOC [1, 2, 4, 21–25]. In the case of Sb_2Te_3 , combined Angle-Resolved Photoemission Spectroscopy (ARPES) and electrical detection experiments provide strong experimental evidence for the existence and manipulability of the helical surface states where electron spin is locked perpendicular to momentum due to strong spin-orbit coupling and time-reversal symmetry [5, 21, 26–31].

We verified this prediction by calculating the spin texture of the rippled supercell with DFT. Fig. 5 displays the spectral weight projected onto the Cartesian spin components (S_x, S_y, S_z).

In the flat 1QL limit at this energy scale, the bands exhibit negligible spin texture due to the hybridization gap. In strong contrast, the rippled heterostructure reveals a vibrant spin texture. As shown in Fig. 5, the bands crossing the Fermi level along the $\Gamma - Y$ direction are strongly polarized in S_x (left panel), while those along $\Gamma - X$ are polarized in S_y (center panel). This orthogonal locking ($k_y \perp S_x, k_x \perp S_y$) is characteristic of Rashba-like interactions, yet the texture is far more complex than a standard Rashba model. The polarization is not confined to a single pair of bands but is distributed across multiple crossing branches, confirming the existence of

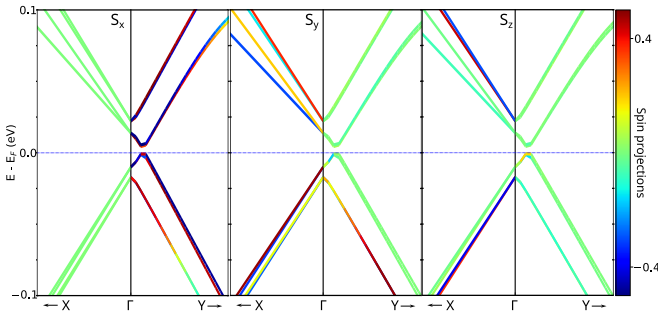


FIG. 5. Spin-texture close to the Dirac cone of the system with ripples. The spin projection axes (S_x, S_y, S_z) coincides with the Cartesian axes.

the helical manifold predicted by our model. The out-of-plane component S_z is negligible along $\Gamma - Y$, but it can be as large 0.5 along $\Gamma - X$, in a strong departure from the Rashba model. While the ripples “smear” the electronic states in momentum space (*i.e.* minibands), it creates a well-defined non-trivial spin-texture, which could be a rich platform for spin-dependent transport [32] despite the lack of a protected topological gap.

V. CONCLUSIONS

In summary, we have presented a comprehensive study of the structural and electronic properties of ultrathin Sb_2Te_3 /graphene heterostructures. Our STM measurements reveal a distinct periodic buckling pattern, which we identify as extrinsic ripples driven by the thermal expansion mismatch between the graphene and the SiO_2 substrate. Motivated by this structural modulation, our theoretical analysis indicates that, far from being a simple structural defect, such rippling could fundamentally alter the electronic landscape of the system. Our density functional theory calculations demonstrate that the hybridization gap of the flat interface (*i.e.* a Dirac-Dirac resonance) is closed by the ripple potential. Through a moiré ladder model and spin-resolved DFT calculations, we established that the system emerges as a “Helical Metal,” characterized by a complex spin texture where the spin polarization remains orthogonal to the carrier momentum along one direction, but it has a strong out-of-plane component along the other. This spin-texture is not reminiscent from the surface states of Sb_2Te_3 –which is effectively spinless in the ultrathin limit– but a new feature arising from the moiré potential.

Moiré modulated SOC entangles spin, sublattice, and leg degrees of freedom, reshaping the miniband structure in momentum space instead of inducing a simple rigid spin splitting. It gives rise to emergent helicity spectral functions that are absent in uniform systems. We found that helicity weight spreads over a dense manifold of moiré minibands, forming an extended network of helicity-carrying states rather than being confined to a few Rashba-like branches. The appearance of Dirac-like

miniband crossings at finite SOC shows that moiré heterostructures can host relativistic quasiparticles via band reconstruction, even when the underlying bands are non-relativistic. Consequently, helicity-resolved static susceptibilities exhibit sharp peaks, revealing strong collective helicity fluctuations already at the bare-response level.

Our findings show that modulated heterostructures constitute an advantageous setting where proximity-induced SOC is not simply transferred from the interface but is significantly enhanced and reshaped through miniband hybridization, thereby strongly favoring the emergence of helical states when additional symmetry-breaking fields or interactions are applied.

ACKNOWLEDGMENTS

C.P. acknowledges support from Fondecyt 1220715, ANID CCTVal CIA250027, ANID SET CTI250019. F.M. acknowledges support from Fondecyt grants 1231487 and 1220715, CEDENNA CIA250002, and partial support by the supercomputing infrastructure of the NLHPC (CCSS210001). P.M. acknowledges support from the Fondo Nacional de Desarrollo Científico y Tecnológico (Fondecyt) under Grant No. 1250122.

Appendix A: Appendixes

1. Experimental Methods

TI/SLG nano-heterostructures based on thin Sb_2Te_3 nanoplatelets were grown on single-layer graphene. Chemical vapor deposition (CVD) growth of single-layer graphene on 25 μm copper foil (>99.8% purity, Alfa Aesar) was carried out at 1050 °C using high-purity CH_4 and H_2 as precursor gases (20 sccm and 10 sccm, respectively). Growth pressure was kept at 0.18 mtorr. After growth, the SLG/copper sample was naturally cooled down in an Ar atmosphere [33]. The resulting SLG on Cu samples was approximately 10 \times 8 cm^2 . Sections of 1 \times 1 cm^2 were cut for the transfer of SLG onto SiO_2 substrates (n-doped, 285 nm oxide thickness) using a PMMA-assisted transfer method [34].

The TI synthesis parameters were tuned to obtain nanostructures thinner than 30 nm in order to promote the presence of surface states and their interaction with the SLG substrate. Sb_2Te_3 NPs were synthesized by a catalyst-free vapor transport and deposition process. Antimony telluride powders (99.999%, Alfa Aesar) were placed on a quartz plate at the center of one zone of the two-zone furnace (TFM2-1200 Across International) while the substrates were placed 11-15 cm downstream from the powder source. Additional variations of synthesis parameters were previously optimized in a separate study [35]. Sb_2Te_3 NPs growth was carried out for 5 min at a temperature of 500 °C and with an Ar flow of 50

sccm. Once the growth is complete, the system was naturally cooled down ($\sim 3.5^\circ\text{C}/\text{min}$), maintaining the Ar flow and a 0.3 torr system pressure. The resulting nano-heterostructures were characterized by low-temperature scanning tunneling microscopy (LT-STM) to obtain information on their structural properties. These experimentally resolved structural features provide the basis for the theoretical analysis presented in this work, which explores the electronic consequences of the observed nanoscale corrugation.

2. Computational Methods

We employed different methods to achieve the best balance between accuracy and computational burden, depending on the specific goal (see below). In general, we used the VASP software [36–39] and PAW pseudopotentials [40].

In Sec. III, to get accurate energetics and energies, we used the functional SCAN+rVV10[41], which provides an accurate description of van der Waals interactions. The kinetic energy cutoff was set to 600 eV, and a 21×21 k-point grid was used. We tested the effects of spin-orbit coupling (SOC) and found it to be negligible for relative energies.

However, in Sec. IV, the attention is shifted to the electronic structure, and then we used a lower accuracy setting as it has been well documented that the Perdew-Ernzenhof-Burke (PBE) [42] correctly describes the low-energy behavior together with a van der Waals correction[43]. The kinetic energy cutoff was lowered to 500 eV. The k-point mesh was $5 \times 3 \times 1$ for the orthogonal supercell and decreased along the long direction when using a supercell.

For the analysis and plotting, we used the pyProcar [44, 45] and Vesta software [46].

To simulate the buckling, we modulated the out-of-plane positions (z) of the heterostructure by $z = h \cos(2\pi y/L)$. With $h = 2.5\text{\AA}$, and L being the ripples wavelength (~ 8.7 nm). The closest value was achieved using a 1×12 supercell.

To capture the shrinking of the unit cell due to the ripples, we changed the corresponding lattice vector to keep the correct distances of the flat graphene layer. The arc length of the graphene layer is

$$L = \int_0^L \sqrt{1 + \left[\frac{2\pi a}{L} \cos\left(\frac{2\pi x}{L}\right) \right]^2} dx \quad (\text{A1})$$

Numerical evaluation gives $\frac{L_0}{L} \approx 1.007$, *i.e.* the unit cell should shrink less than 1% to avoid extra strain due the ripples.

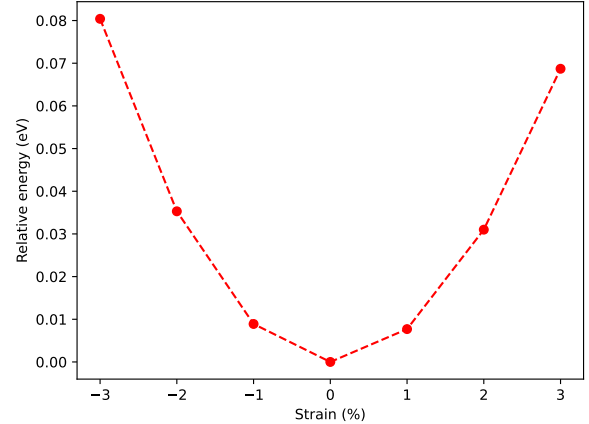


FIG. 6. Energy of a single QL of Sb_2Te_3 as a function of biaxial strain. The energy of the minimum energy system is set to zero.

3. Energy considerations

According to DFT calculations, the distance between graphene and Sb_2Te_3 is 3.59\AA , which is typical for van der Waals (vdW) heterostructures. The measured samples preserve the periodicity of the unit cell along one direction; this aspect is not considered further in the present discussion. In the orthogonal direction, the samples exhibit a periodicity of $L \approx 8.7$ nm, corresponding to approximately 20 or 21 unit cells of Sb_2Te_3 . The binding energy (E_B) between graphene and single Sb_2Te_3 QL, $E_B = E_{\text{total}} - E_{\text{graphene}} - E_{\text{Sb}_2\text{Te}_3} = 0.23$ eV per cell (*i.e.* the cell from Fig. 1b). The variation in E_B resulting from a lateral shift between the two materials is less than 0.01 eV per cell. Consequently, in the absence of point defects, the energy required to slide the layers relative to each other is negligible compared to thermal energy at room temperature. The change in energy of the Sb_2Te_3 monolayer under biaxial strain, as shown in Fig. 6, is also negligible (0.01 eV per unit cell) for a strain of 1%. Uniaxial strain is expected to result in even lower stress. Since the energy penalty for sliding is less than 0.01 eV, and both energy penalties are an order of magnitude smaller than E_B , significant strain accumulation is unlikely.

In a perfectly homogeneous material, the total strain energy is ~ 30 meV, corresponding to each unit cell being subjected to a 0.35% strain. Since the system is free to slide, the actual strain energy may be lower. This value is negligible compared with the binding energy ($E_B = 0.23$ eV per unit cell). To further evaluate the energy cost associated with potential buckling, we consider the buckling amplitude $z(y) = \alpha \cos\left(\frac{2\pi y}{L}\right)$. Here, $2\alpha \approx 5.0\text{\AA}$ represents the observed height difference. The variable y denotes the direction of the stripes. The minimum curvature radius (R) occurs at $y = 0$, and the corresponding

curvature ($\kappa = R^{-1}$) $\kappa = \frac{|z''|}{(1+z'^2)^{3/2}} \sim 0.013 \text{ \AA}^{-1}$. The bending energy per atom, $E_{bend} = \frac{C_b k^2}{2}$, is determined by the material's bending modulus. For graphene, $C_b = 3.43 \text{ eV/\AA}^2$ per atom [47], which yields a total bending energy of $E_{bend} \approx 0.02 \text{ eV}$ per graphene strip. While Sb_2Te_3 quintuple layers exhibit anisotropy, a reasonable estimate can be made by applying the bending energy expression for homogeneous materials, $E_{bend} = \frac{Y t^2 \kappa^2}{2}$, where Y denotes Young's modulus and t represents the material thickness. The t^2 dependence indicates that bending Sb_2Te_3 is considerably more challenging than bending graphene. The bending modulus of the transition metal dichalcogenide MoS_2 is approximately ten times greater than that of graphene ($C_b \approx 45 \text{ eV/\AA}^2$ per atom [47]). Although Sb_2Te_3 and MoS_2 differ in several properties, this value provides a reasonable approximation because Sb_2Te_3 is more than twice as thick as MoS_2 , and in nanofilm experiments, the Young's modulus of Sb_2Te_3 is about five times smaller than that of MoS_2 . These two factors are expected to compensate for each other, leading to an estimated bending energy of $E_{bend} = 0.2 \text{ eV}$ per stripe.

The bending energy is expected to be similar to the stress induced by the mismatch. Disregarding any relative sliding, a buckling pattern should induce both compression and elongation, overall increasing the stress. Therefore, the observed ripples are not caused by an intrinsic instability of the freestanding Graphene/ Sb_2Te_3 heterostructure. On the other hand, the bending energy at the minimum curvature radius is similar to the binding energy, $E_B - E_{bend} \geq 0$, thus separation of the two two-dimensional materials is ruled out; if buckling occurs, both subsystems remain together. Additionally, Sb_2Te_3 samples thicker than 1QL are expected to either separate from graphene or flatten it, as E_{bend} increases quadratically with the sample thickness.

An alternative explanation for stripe formation is that the system exhibits thickness variations along the stripes. These variations could result in distinct material phases. Lateral coexistence of different phases requires that the process be energetically favorable. This requirement implies that the binding energy between graphene and the Sb_2Te_3 QL should increase across regions of varying thickness. The system must also compensate for the energy cost associated with lateral defects or interface reconstructions between the two SbTe-based phases. The unknown phase is likely strained by the graphene layer, which is necessary to explain the observed transition between the two phases; otherwise, only the lower-energy phase would be present. The formation of stripes supports the existence of a periodic strain field. Furthermore, an energy barrier must be present to prevent sliding, as its absence would inhibit the accumulation of strain. This hypothesis is also applicable to other materials. Several structurally distinct phases are observed for chalcogens and pnictogens, each characterized by unique atomic arrangements and stoichiometries. The

most prevalent among these are layered structures containing interwoven Bi_2 interlayers [48, 49]. These phases can coexist within a single sample [50]. Thinner phases of As_2Se_3 , distinguished by more complex geometries, have also been identified [51]. Additionally, unusual forms, such as a square BiTe monolayer phase, have been reported on Bi_2Te_3 [52]. Of particular relevance is a high-pressure-induced rectangular crystal phase of BiS_2 and BiSe_2 [53, 54]. The freestanding monolayer of SbTe_2 , referred to as r- SbTe_2 , is predicted to be stable in its distorted rectangular geometry [55]. However, a simple analysis shows that the combined energetic penalties from higher formation energy and increased phase-boundary costs are challenging to overcome with a modest binding-energy enhancement in our case. This conclusion is further supported by two additional considerations related to phase behavior. First, the hypothesis that stripes arise from different $\text{Sb}_x\text{Te}_{1-x}$ phases separated by boundaries would require those boundaries to be pinned by a substantial energy barrier, which is at odds with our earlier finding of minimal sliding resistance between layers. Second, the gently undulating features observed by STM suggest mechanical buckling, as opposed to the sharp, step-like transitions expected at lateral phase boundaries between distinct $\text{Sb}_x\text{Te}_{1-x}$ phases. Together, these observations rule out the coexistence of distinct $\text{Sb}_x\text{Te}_{1-x}$ phases as a likely explanation for the stripes.

For the sake of completeness, long molecular dynamics simulations were conducted using a DFT-based force field for various arrangements and strain values on the Sb_2Te_3 QL. The system was allowed to evolve freely, subject only to periodic boundary conditions. In all cases, neither bending, buckling, nor stripe formation was observed.

4. Moiré ladder model for modulated Sb_2Te_3 /SLG

In this appendix, we analyze a simplified model to assess the impact of ripple-induced moiré modulation on the spectrum of a spin-orbit-coupled heterostructure. We model Sb_2Te_3 1QL/SLG heterostructures as a ladder system, where the top and bottom legs represent the top and bottom surfaces of the heterostructure, as illustrated in Fig.7(a). The ladder consists of two coupled legs, each with two sites (A and B representing Sb and Te atoms) per unit cell. The composite ladder unit cell contains a total of four sites $\{A_1, B_1, A_2, B_2\}$ (subscripts 1, 2 label legs). The composite cell has a length equal to $2a$, and the original reciprocal period is $G_0 = \pi/a$. In our effective description, the structural ripples of the Sb_2Te_3 film enter through a long-wavelength modulation of the interleg hopping and a slight dimerization in leg two. In real space, this modulation is $t_{\perp}(n) \sim \cos(2\pi\delta n)$, where n is the site index along the ladder direction and $\delta = p/q \in (0, 1)$ is a positive dimensionless parameter that determines the period of the modulation. In addition, $\delta \sim 1$ controls the weak dimerization in leg 2 which

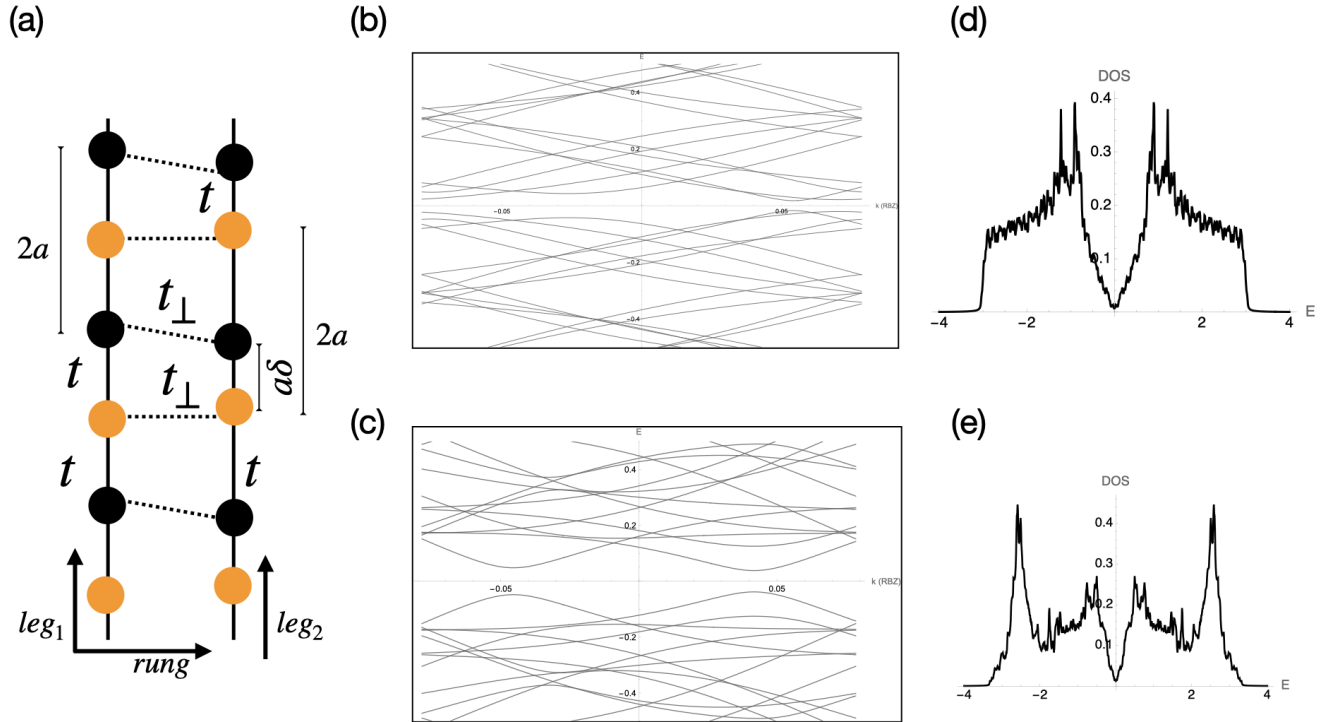


FIG. 7. (a) The moiré ladder model. (b,c) Spectrum of the minibands of the ladder model in the RBZ with $\delta = \frac{17}{20}$ and $\alpha = t$ without (b) and with (c) spin orbit coupling. (d) DOS at $T=0$ of a spinless system with $\delta = \frac{19}{20}$ and (e) a spinful system with spin orbit coupling, $\alpha = t$ and at $\delta = \frac{19}{20}$.

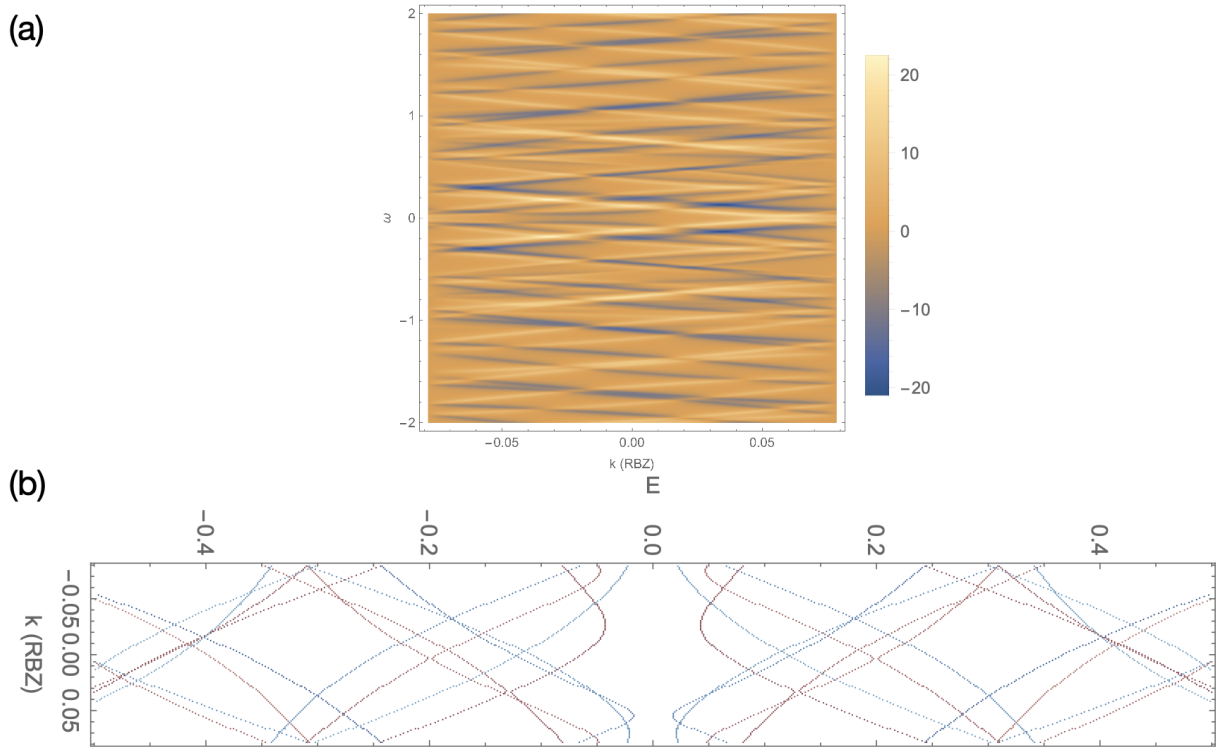


FIG. 8. (a) Helical spectral function of the ladder model at $\delta = \frac{19}{20}$, $\alpha = t$ and $T = 0$. (b) zoom out of the minibands spectrum close to the fermi energy ($E=0$) at $\delta = \frac{19}{20}$ and $\alpha = t$. The colors of the minibands reflect their helicity weight.

gives rise to a Peierls phase in this leg. This choice reflects the fact that the ripple profile modulates the local bonding environment of leg 2 of the model (representing the interface-facing side of the quintuple layer), while leg 1 remains undimerized. Intraleg hopping occurs between nearest-neighbor atoms, and its amplitude is t .

To relate δ to the physical ripple wavelength λ_{ripple} , we match the modulation wavevector to the ripple wavevector $Q_{\text{ripple}} = 2\pi/\lambda_{\text{ripple}}$. Since the dimensionless ratio of the two wavevectors is $\delta = \frac{Q_{\text{ripple}}}{G_0} = \frac{2\pi/\lambda_{\text{ripple}}}{\pi/a} = \frac{2a}{\lambda_{\text{ripple}}}$, it follows that $\lambda_{\text{ripple}} = \frac{2a}{\delta}$. To render the modulation commensurate, we choose $\delta = p/q$ with p and q coprime. Interleg modulation and the dimerization of leg-2 are periodic after q unit cells, so that one ripple period spans q unit cells and has physical length $\lambda_{\text{ripple}} = \frac{2aq}{p}$. For instance, for $\delta = 0.95$ ($p = 19$, $q = 20$), the resulting supercell contains 20 unit cells and the ripple wavelength is $\lambda_{\text{ripple}} \simeq 40a$, consistent with the mesoscopic ($\sim 5\text{--}20\text{ nm}$) corrugation length scales observed experimentally in Sb_2Te_3 /graphene heterostructures. Henceforth, we choose a , half the legs lattice constant, as the length unit.

The relative mismatch between legs yields a moiré supercell of q composite cells of $4q$ sites, a moiré reciprocal vector in the reduced Brillouin zone (RBZ) $b_s = \frac{G_0}{q} = \frac{\pi}{q}$, and a real-space supercell of length $L_s = 2q$. Rung tunneling occurs between the same sublattice, and its average is t . Schrieffer-Wolff perturbation theory [56] gives rise to a first-harmonic of amplitude $t_1 = (1 - \delta)t$ modulated by the envelope $t_{\perp}(n) = t + t_1 \cos\left(\frac{2\pi n}{q}\right)$. Throughout, we choose t as our energy scale.

Structure factors associated with hopping in leg-1 and leg-2 are respectively $C(k) = 2 \cos k$, $C_{\delta}(k) = 2 \cos(k - \pi\delta)$, and the Peierls phase from the dimerization of leg-2 is $\phi(k) = k(1 - \delta) + \pi\delta$. In Fourier space, the moiré rung modulation becomes $t_{\perp}(k) = 1 + (1 - \delta) \cos(qk)$. Throughout, we choose t as our energy scale.

In graphene-based heterostructures coupled to a topological insulator, a perpendicular electric field is induced, and the dominant proximity-induced SOC is generally of Rashba character [57–59]. In a quasi-one-dimensional lattice description, the Rashba SOC generated by a perpendicular electric field $\mathbf{E} = E_z \hat{z}$ takes the form

$$H_{\text{SOC}} = \alpha \sum_j \left(c_{j+1}^{\dagger} i\sigma_y c_j - c_j^{\dagger} i\sigma_y c_{j+1} \right), \quad (\text{A2})$$

where the fermion operators $c_j = (c_{j\uparrow}, c_{j\downarrow})^T$ and σ_y act on spin. Fourier transforming Eq. (A2), one obtains

$$H_{\text{SOC}}^{(1)} = 2i\alpha \sum_k (\sin k) c_k^{\dagger} \sigma_y c_k. \quad (\text{A3})$$

In a uniform system such as leg-1, the SOC term in Eq. A3 appears as a momentum-odd contribution, which vanishes at time-reversal invariant momenta and reflects the inversion-symmetry breaking at the interface. In leg-2 the the hopping paths of electrons are modulated in real space, and as a result, the SOC term on that leg acquires a phase,

$$H_{\text{SOC}}^{(2)} = \alpha \sum_j \left(e^{-i\pi\delta} c_{j+1,2}^{\dagger} i\sigma_y c_{j,2} - e^{+i\pi\delta} c_{j,2}^{\dagger} i\sigma_y c_{j+1,2} \right),$$

Fourier transforming the previous equation yields

$$H_{\text{SOC}}^{(2)} = 2i\alpha \sum_k e^{i\phi(k)} \sin(k - \pi\delta) c_{k,2}^{\dagger} \sigma_y c_{k,2}. \quad (\text{A4})$$

with α the SOC strength and σ_y the second Pauli matrix. We define the spinor as the eight-component object, $\Psi_k = (c_{1A\uparrow}, c_{1A\downarrow}, c_{1B\uparrow}, c_{1B\downarrow}, c_{2A\uparrow}, c_{2A\downarrow}, c_{2B\uparrow}, c_{2B\downarrow})$ and we assign opposite helicity to the two legs, such that leg 1 carries helicity $+\sigma_y$ (upper surface) and leg 2 carries helicity $-\sigma_y$ (lower surface). The total Hamiltonian, including both the kinetic terms and the opposite-helicity spin-orbit coupling, yields

$$H(k) = \begin{pmatrix} 0 & 0 & C(k) & -iS(k) & t_{\perp}(k) & 0 & 0 & 0 \\ 0 & 0 & iS(k) & C(k) & 0 & t_{\perp}(k) & 0 & 0 \\ C(k) & -iS(k) & 0 & 0 & 0 & 0 & t_{\perp}(k) & 0 \\ iS(k) & C(k) & 0 & 0 & 0 & 0 & 0 & t_{\perp}(k) \\ t_{\perp}(k) & 0 & 0 & 0 & 0 & 0 & C_{\delta}(k) e^{i\phi(k)} & iS_{\delta}(k) e^{i\phi(k)} \\ 0 & t_{\perp}(k) & 0 & 0 & 0 & 0 & -iS_{\delta}(k) e^{-i\phi(k)} & C_{\delta}(k) e^{i\phi(k)} \\ 0 & 0 & t_{\perp}(k) & 0 & C_{\delta}(k) e^{-i\phi(k)} & iS_{\delta}(k) e^{i\phi(k)} & 0 & 0 \\ 0 & 0 & 0 & t_{\perp}(k) & -iS_{\delta}(k) e^{-i\phi(k)} & C_{\delta}(k) e^{-i\phi(k)} & 0 & 0 \end{pmatrix}, \quad (\text{A5})$$

where $S(k) = 2\alpha \sin k$ and $S_{\delta}(k) = 2\alpha \sin(k - \pi\delta)$. Eq. A5 is given in the extended Brillouin zone (EBZ), $k \in (-qG_0, qG_0)$, with reciprocal superlattice $G_m = \{mqG_0 \mid m \in \mathbb{Z}\}$. For a given δ , the similarity transformation $\Delta = \pi q$ applied to $H(k)$ imposes constraints

on p and q that determine the generic global period $2\pi q$ giving rise to EBZ [60]. In the absence of SOC, the spectrum obeys $E(k) = E(k + G_m)$. Once SOC is introduced, the Hamiltonian acquires momentum-odd contributions $\propto \sin(k - \pi\delta) \sigma_y$, which reverse sign under $k \rightarrow k + G_m$.

Consequently, translation by G_m alone ceases to be a symmetry, and the Hamiltonian remains invariant under the combined action of a moiré translation and a π spin rotation about the y axis. Because this composite symmetry squares to a translation by $2G_m$, the spectral periodicity in the extended Brillouin zone is effectively halved.

The reduced first Brillouin zone of the moiré lattice (RBZ) spans the interval $(-b_s/2, b_s/2)$, and the reciprocal superlattice $G_s = \{m b_s \mid m \in \mathbb{Z}\}$. To build the Hamiltonian of the system in the RBZ we keep the q replica momenta $\{\bar{k} + mG_s\}_{m=0}^{q-1}$ in the Hamiltonian matrix H_{RBZ} . Thus, the block-diagonal piece becomes $[H_{\text{RBZ}}^{(0)}(\bar{k})]_{mm'} = \delta_{mm'} H(\bar{k} + mG_s)$, $m, m' = 0, \dots, q-1$. Rung modulation $\cos(qk)$ connects nearest-neighbor replicas in the RBZ and gives rise to the off-diagonal part $[\delta H_{\text{RBZ}}(\bar{k})]_{m, m \pm 1} = \frac{t_1}{2} R$, $R = \sigma_1 \otimes \mathbb{I}_2$, where σ_j is the j -th Pauli matrix. The $4q \times 4q$ moiré Hamiltonian in the RBZ becomes [60] $H_{\text{RBZ}}(\bar{k}) = H_{\text{RBZ}}^{(0)}(\bar{k}) + \delta H_{\text{RBZ}}(\bar{k})$. If $t_1 = 0$ the $4q$ bands split into q independent copies of the four parent bands. The symmetry of H is preserved by H_{RBZ} [60]. Fig.7(b,c) shows a zoomed-out view of the energy spectra of the minibands in the reduced Brillouin zone at $\delta = 0.95$ and $\delta = 0.85$ in the absence and presence of spin-orbit coupling. Without SOC, the spectrum consists of multiple folded minibands that intersect extensively, reflecting both the moiré backfolding and the underlying spin degeneracy. Fig.7(c) shows that SOC lifts spin degeneracy, and a large fraction of the band crossings is replaced by avoided crossings. This reconstruction reflects the entanglement of spin and moiré degrees of freedom induced by SOC and leads to a redistribution of spectral weight across the miniband manifold as predicted by our DFT calculations presented above. With a perfect match between the legs ($\delta = 1$), the density of states depicts a pair of van Hove singularities (VHS) at the edges of the bands, a finite density of states at all energies, and another pair of VHS at $E = \pm t_1$, signaling the coupling between the two legs [60]. Once $\delta \neq 1$, the moiré potential smears out the peaks at the edges of the spectra; the VHS at $E = \pm t$ splits into two peaks about $E \sim \pm t_1$ due to the breaking of inversion symmetry Fig.7(d) [61]. Including SOC, Fig.7(e) removes spin degeneracy, opening gaps at many band crossings, redistributing spectral weight by increasing the population of states close to the Fermi level and producing a qualitatively altered DOS.

The Dirac-like crossings observed in Fig.7(c) indicate that the moiré-modulated SOC not only lifts degeneracies but also reorganizes the miniband structure into effective two-band sectors with linear dispersion. The case at $\delta = \frac{17}{20}$ illustrates how moiré modulation and SOC jointly induce emergent relativistic behavior in otherwise heavily folded miniband spectra. With SOC present, a pure moiré translation by a reciprocal lattice vector G_m ceases

to be a symmetry. Nevertheless, the Hamiltonian is invariant under the composite operation $\tilde{T} = T_{G_m} \mathcal{R}_y(\pi)$, with $\mathcal{R}_y(\pi) = -i\sigma_y$ denoting a π spin rotation about the SOC-defined axis. \tilde{T} acts as a quantum number that differentiates miniband eigenstates, such that bands with distinct \tilde{T} eigenvalues cannot hybridize at the same momentum. As a result, when moiré folding brings bands from different \tilde{T} sectors into contact, SOC imposes symmetry-protected linear crossings, yielding Dirac-like nodes in the miniband spectrum.

Consider the helicity operator as the difference between the spin densities on the two legs [62], $\Gamma_{\text{hel}} = S_y^{(1)} - S_y^{(2)}$, where $S_y^{(\ell)} = \sum_k c_{k,\ell}^\dagger \sigma_y c_{k,\ell}$, with σ_y acting in spin space. Γ_{hel} quantifies how unevenly spin polarization along the SOC-determined axis is shared between the two legs. It is antisymmetric under leg exchange, invariant under time reversal, and zero when SOC is absent due to spin-rotation symmetry.

To find out whether helical states are plausible in graphene/Sb₂Te₃ thin films, at the single-particle level, we compute the dynamical spectral function using Lorentzian broadening: $A_\Gamma(k, \omega) = \sum_n |\langle n, k | \Gamma | n, k \rangle|^2 \frac{\eta}{(\omega - E_{n,k})^2 + \eta^2}$, where η is a small positive broadening. The helicity-resolved spectral function offers a direct probe of how proximity-induced spin-orbit coupling is redistributed throughout the moiré minibands. Without spin-orbit coupling, spin-rotation symmetry enforces the helicity-resolved spectral function to be zero. Upon introducing SOC, Fig.8(a) reveals a dense mesh of oblique streaks with alternating blue and white intensities, spanning the reduced Brillouin zone. Each streak represents a miniband branch with nonzero helicity weight, where the color encodes both the sign and magnitude of the expectation value of the helicity operator Γ_{hel} . The tilted alignment of these features arises from the finite group velocity of the associated states, and the alternating sign directly evidences spin-momentum locking: minibands with opposite dispersion slopes possess opposite helicity, as enforced by time-reversal symmetry.

Unlike uniform Rashba systems, where helicity is restricted to a few well-defined branches, the model shows that the moiré potential distributes helicity across numerous minibands. The color-coded miniband structure in the RBZ in Fig.8(b) shows that every miniband branch in the reduced Brillouin zone carries a nonzero helicity weight. The simultaneous presence of positive and negative helicity on different branches reflects the odd-momentum character of the SOC and the maintenance of time-reversal symmetry. Fig.8b shows that fluctuations in the helicity order parameter can be derived from an extensive set of particle-hole excitations involving all minibands, making the system intrinsically prone to helical collective behavior.

[1] J. Kiemle, L. Powalla, K. Polyudov, L. Gulati, M. Singh, A. W. Holleitner, M. Burghard, and C. Kastl, Gate-tunable helical currents in commensurate topological insulator/graphene heterostructures, *ACS nano* **16**, 12338 (2022).

[2] K. Song, D. Soriano, A. W. Cummings, R. Robles, P. Ordejón, and S. Roche, Spin proximity effects in graphene/topological insulator heterostructures, *Nano letters* **18**, 2033 (2018).

[3] J. Chae, S.-H. Kang, S. H. Park, H. Park, K. Jeong, T. H. Kim, S.-B. Hong, K. S. Kim, Y.-K. Kwon, J. W. Kim, and M.-H. Cho, Closing the surface bandgap in thin bi₂se₃/graphene heterostructures, *ACS Nano* **13**, 3931 (2019).

[4] K. Zollner and J. Fabian, Proximity effects, topological states, and correlated physics in graphene heterostructures, *2D Materials* **12**, 013004 (2024).

[5] Y. Yin, G. Wang, C. Liu, H. Huang, J. Chen, J. Liu, D. Guan, S. Wang, Y. Li, C. Liu, *et al.*, Moiré-pattern-modulated electronic structures in sb₂te₃/graphene heterostructure, *Nano Research* **15**, 1115 (2022).

[6] K. Yang, Z. Xu, Y. Feng, F. Schindler, Y. Xu, Z. Bi, B. A. Bernevig, P. Tang, and C.-X. Liu, Topological minibands and interaction driven quantum anomalous hall state in topological insulator based moiré heterostructures, *Nature Communications* **15**, 2670 (2024).

[7] M. Salvato, M. D. Crescenzi, M. Scagliotti, P. Casttrucci, S. Boninelli, G. M. Caruso, Y. Liu, A. Mikkelsen, R. Timm, S. Nahas, A. Black-Schaffer, G. Kunakova, J. Andzane, D. Ert, T. Bauch, and F. Lombardi, Nanometric moiré stripes on the surface of bi₂se₃ topological insulator, *ACS Nano* **16**, 13860 (2022).

[8] H. Zhang, C.-X. Liu, X.-L. Qi, X. Dai, Z. Fang, and S.-C. Zhang, Topological insulators in bi₂se₃, bi₂te₃ and sb₂te₃ with a single dirac cone on the surface, *Nature Physics* **5**, 438 (2009).

[9] Y. Zhang, K. He, C.-Z. Chang, C.-L. Song, L.-L. Wang, X. Chen, J.-F. Jia, Z. Fang, X. Dai, W.-Y. Shan, S.-Q. Shen, Q. Niu, X.-L. Qi, S.-C. Zhang, X.-C. Ma, and Q.-K. Xue, Crossover of the three-dimensional topological insulator bi₂se₃ to the two-dimensional limit, *Nature Physics* **6**, 584 (2010).

[10] P. Giraldo-Gallo, Y. Zhang, C. Parra, H. C. Manoharan, M. R. Beasley, T. H. Geballe, M. J. Kramer, and I. R. Fisher, Stripe-like nanoscale structural phase separation in superconducting BaPb(1-x)Bi(x)O₃, *Nat. Commun.* **6**, 8231 (2015).

[11] D. Yoon, Y.-W. Son, and H. Cheong, Negative thermal expansion coefficient of graphene measured by raman spectroscopy, *Nano Lett.* **11**, 3227 (2011).

[12] J. Mao, S. P. Milovanović, M. Andelković, X. Lai, Y. Cao, K. Watanabe, T. Taniguchi, L. Covaci, F. M. Peeters, A. K. Geim, Y. Jiang, and E. Y. Andrei, Evidence of flat bands and correlated states in buckled graphene superlattices, *Nature* **584**, 215 (2020).

[13] V. E. Calado, G. F. Schneider, A. M. M. G. Theulings, C. Dekker, and L. M. K. Vandersypen, Formation and control of wrinkles in graphene by the wedging transfer method, *Applied Physics Letters* **101**, 103116 (2012), https://pubs.aip.org/aip/apl/article-pdf/doi/10.1063/1.4751982/14254838/103116_1_online.pdf.

[14] I. Mohelsky, J. Wyzula, F. Le Mardelé, F. Abadizaman, O. Caha, A. Dubroka, X. D. Sun, C. W. Cho, B. A. Piot, M. F. Tazim, I. Aguilera, G. Bauer, G. Springholz, and M. Orlita, Electronic band structure of sb₂te₃, *Phys. Rev. B* **109**, 165205 (2024).

[15] K.-H. Jin and S.-H. Jhi, Proximity-induced giant spin-orbit interaction in epitaxial graphene on a topological insulator, *Phys. Rev. B* **87**, 075442 (2013).

[16] G. Bian, T.-F. Chung, C. Chen, C. Liu, T.-R. Chang, T. Wu, I. Belopolski, H. Zheng, S.-Y. Xu, D. S. Sanchez, N. Alidoust, J. Pierce, B. Quilliams, P. P. Barletta, S. Lorcy, J. Avila, G. Chang, H. Lin, H.-T. Jeng, M.-C. Asensio, Y. P. Chen, and M. Z. Hasan, Experimental observation of two massless dirac-fermion gases in graphene-topological insulator heterostructure, *2D Materials* **3**, 021009 (2016).

[17] T. Naimer and J. Fabian, Twist-angle dependent proximity induced spin-orbit coupling in graphene/topological insulator heterostructures, *Phys. Rev. B* **107**, 195144 (2023).

[18] J. Zhang, C. Triola, and E. Rossi, Proximity effect in graphene-topological-insulator heterostructures, *Physical review letters* **112**, 096802 (2014).

[19] Z. Lin, W. Qin, J. Zeng, W. Chen, P. Cui, J.-H. Cho, Z. Qiao, and Z. Zhang, Competing gap opening mechanisms of monolayer graphene and graphene nanoribbons on strong topological insulators, *Nano Letters* **17**, 4013 (2017).

[20] R. Banerjee, V.-H. Nguyen, T. Granzier-Nakajima, L. Pabbi, A. Lherbier, A. R. Binion, J.-C. Charlier, M. Terrones, and E. W. Hudson, Strain modulated superlattices in graphene, *Nano Letters* **20**, 3113 (2020).

[21] Y. Takagaki, Y. Saito, and J. Tominaga, Manipulation of the presence of helical surface states of topological insulators using sb₂te₃-gete superlattices, *Applied Physics Letters* **108** (2016).

[22] D. Khokhriakov, A. M. Hoque, B. Karpak, and S. P. Dash, Gate-tunable spin-galvanic effect in graphene-topological insulator van der waals heterostructures at room temperature, *Nature communications* **11**, 3657 (2020).

[23] H. Li, H. Zhang, J. Shao, Y. Zhang, D. Yao, and G. Yang, Topological insulator-graphene junction for spin transport, *Applied Physics Letters* **101** (2012).

[24] M. A. Hoque, L. Sjöström, D. Khokhriakov, B. Zhao, and S. P. Dash, Room temperature nonlocal detection of charge-spin interconversion in a topological insulator, *npj 2D Materials and Applications* **8**, 10 (2024).

[25] Y. Tanabe, N. H. Tu, M.-C. Jiang, Y. L. Chiew, M. Haruta, K. Adachi, D. Pomaranski, R. Ito, Y. Shimazaki, D. Hashizume, *et al.*, High-temperature helical edge states in bisbte₃ -2/graphene van der waals heterostructure, *arXiv preprint arXiv:2506.20510* (2025).

[26] C. Li, O. van 't Erve, Y. Li, L. Li, and B. Jonker, Electrical detection of the helical spin texture in a p-type topological insulator sb₂te₃, *Scientific reports* **6**, 29533 (2016).

[27] Y. Takagaki, A. Giussani, K. Perumal, R. Calarco, and K.-J. Friedland, Robust topological surface states in sb₂te₃ layers as seen from the weak antilocalization effect, *Physical Review B—Condensed Matter and Mate-*

rials Physics **86**, 125137 (2012).

[28] K. Zollner and J. Fabian, Heterostructures of graphene and topological insulators bi_2se_3 , bi_2te_3 , and sb_2te_3 , physica status solidi (b) **258**, 2000081 (2021).

[29] D. Zhao, X. Wang, X. Wang, X. Wang, X. He, Y. Fu, D. J. Singh, and L. Zhang, Layer stacking-induced transition to a kane-band semiconductor in sb_2te_3 , The Journal of Physical Chemistry C **128**, 17081 (2024).

[30] L. Locatelli, A. Kumar, P. Tsipas, A. Dimoulas, E. Longo, and R. Mantovan, Magnetotransport and arpes studies of the topological insulators sb_2te_3 and bi_2te_3 grown by mocvd on large-area si substrates, Scientific reports **12**, 3891 (2022).

[31] A. Manchon, H. C. Koo, J. Nitta, S. M. Frolov, and R. A. Duine, New perspectives for rashba spin–orbit coupling, Nature materials **14**, 871 (2015).

[32] A. Bordoloi, A. C. Garcia-Castro, Z. Romestan, A. H. Romero, and S. Singh, Promises and technological prospects of two-dimensional rashba materials, Journal of Applied Physics **135**, 220901 (2024).

[33] C. Parra, F. Montero-Silva, D. Gentil, V. Del Campo, T. Henrique Rodrigues da Cunha, R. Henríquez, P. Häberle, C. Garín, C. Ramírez, R. Fuentes, M. Flores, and M. Seeger, The many faces of graphene as protection barrier. performance under microbial corrosion and ni allergy conditions, Materials (Basel) **10**, 1406 (2017).

[34] C. Parra, J. Aristizabal, B. Arce, F. Montero-Silva, S. Lascano, R. Henriquez, P. Lazcano, P. Giraldo-Gallo, C. Ramírez, T. Henrique Rodrigues da Cunha, and A. Barrera de Brito, Graphene coating as an effective barrier to prevent bacteria-mediated dissolution of gold, Metals (Basel) **11**, 147 (2021).

[35] V. Gallardo, B. Arce, F. Muñoz, R. San Martín, I. Zubritskaya, P. Giraldo-Gallo, C. Z. Zerger, H. C. Manoharan, and C. Parra, Exploring structural and electronic properties of topological insulator/graphene nano-heterostructures, Results in Physics **67**, 108058 (2024).

[36] G. Kresse and J. Hafner, Ab initio molecular dynamics for liquid metals, Phys. Rev. B **47**, 558(R) (1993).

[37] G. Kresse and J. Hafner, Ab initio molecular-dynamics simulation of the liquid-metal–amorphous-semiconductor transition in germanium, Phys. Rev. B **49**, 14251 (1994).

[38] G. Kresse and J. Furthmüller, Efficiency of ab-initio total energy calculations for metals and semiconductors using a plane-wave basis set, Comput. Mater. Sci. **6**, 15 (1996).

[39] G. Kresse and J. Furthmüller, Efficient iterative schemes for ab initio total-energy calculations using a plane-wave basis set, Phys. Rev. B **54**, 11169 (1996).

[40] G. Kresse and D. Joubert, From ultrasoft pseudopotentials to the projector augmented-wave method, Phys. Rev. B **59**, 1758 (1999).

[41] H. Peng, Z.-H. Yang, J. P. Perdew, and J. Sun, Versatile van der waals density functional based on a meta-generalized gradient approximation, Phys. Rev. X **6**, 041005 (2016).

[42] J. P. Perdew, K. Burke, and M. Ernzerhof, Generalized gradient approximation made simple, Phys. Rev. Lett. **77**, 3865 (1996).

[43] S. Grimme, S. Ehrlich, and L. Goerigk, Effect of the damping function in dispersion corrected density functional theory, Journal of Computational Chemistry **32**, 1456 (2011).

[44] U. Herath, P. Tavadze, X. He, E. Bousquet, S. Singh, F. Muñoz, and A. H. Romero, Pyprocar: A python library for electronic structure pre/post-processing, Comput. Phys. Commun. **251**, 107080 (2019).

[45] L. Lang, P. Tavadze, A. Tellez, E. Bousquet, H. Xu, F. Muñoz, N. Vasquez, U. Herath, and A. H. Romero, Expanding pyprocar for new features, maintainability, and reliability, Computer Physics Communications **297**, 109063 (2024).

[46] K. Momma and F. Izumi, Vesta 3 for three-dimensional visualization of crystal, volumetric and morphology data, Journal of applied crystallography **44**, 1272 (2011).

[47] R. I. González, F. J. Valencia, J. Rogan, J. A. Valdivia, J. Sofo, M. Kiwi, and F. Munoz, Bending energy of 2d materials: graphene, mos2 and imogolite, RSC Adv. **8**, 4577 (2018).

[48] Y. Kim, S. Cho, A. DiVenere, G. K. L. Wong, and J. B. Ketterson, Composition-dependent layered structure and transport properties in bite thin films, Phys. Rev. B **63**, 155306 (2001).

[49] J. W. G. Bos, H. W. Zandbergen, M.-H. Lee, N. P. Ong, and R. J. Cava, Structures and thermoelectric properties of the infinitely adaptive series $(\text{Bi}_2)_m(\text{Bi}_2\text{Te}_3)_n$, Phys. Rev. B **75**, 195203 (2007).

[50] S. Drzewowska and B. Onderka, Different approach to thermodynamic description of bi-te binary system, Journal of Phase Equilibria and Diffusion **44**, 429 (2023).

[51] L. Lityagina, L. Kulikova, I. Zibrov, T. Dyuzheva, N. Nikolaev, and V. Brazhkin, Structural transformations in the as–se system under high pressures and temperatures, Journal of Alloys and Compounds **644**, 799 (2015).

[52] Z.-W. Wang, W.-K. Huang, K.-W. Zhang, D.-J. Shu, M. Wang, and S.-C. Li, Aggregation of bite monolayer on $\text{bi}_2\text{te}_3(111)$ induced by diffusion of intercalated atoms in the van der waals gap, Phys. Rev. B **95**, 121403 (2017).

[53] A. Yamamoto, D. Hashizume, M. S. Bahramy, and Y. Tokura, Coexistence of monochalcogen and dichalcogen ions in bise2 and bis2 crystals prepared at high pressure, Inorganic Chemistry **54**, 4114 (2015).

[54] S. M. Kevy, M. B. Nielsen, L. F. Lundgaard, D. Ceresoli, Y.-S. Chen, H. Reardon, P. Parisiades, and M. Bremholm, Investigation of the high pressure phase bis2: Temperature-resolved structure and compression behavior to 60 gpa, Journal of Alloys and Compounds **789**, 588 (2019).

[55] J. D. Mella, M. Nalabothula, F. Muñoz, K. M. Rabe, L. Wirtz, S. Singh, and A. H. Romero, Prediction of bis2-type pnictogen dichalcogenide monolayers for optoelectronics, npj 2D Materials and Applications **8**, 4 (2024).

[56] J. R. Schrieffer and P. A. Wolff, Relation between the anderson and kondo hamiltonians, Phys. Rev. **149**, 491 (1966).

[57] G. Bihlmayer, P. Noël, D. V. Vyalikh, E. V. Chulkov, and A. Manchon, Rashba-like physics in condensed matter, Nature Reviews Physics **4**, 642 (2022).

[58] I. Ado, O. A. Tretiakov, and M. Titov, Microscopic theory of spin-orbit torques in two dimensions, Physical Review B **95**, 094401 (2017).

[59] L. Chen, M. Gmitra, M. Vogel, R. Islinger, M. Kronseeder, D. Schuh, D. Bougeard, J. Fabian, D. Weiss, and C. Back, Electric-field control of interfacial spin–orbit fields, Nature Electronics **1**, 350 (2018).

[60] P. Mellado, F. Muñoz, and J. Cabezas-Escarez, Sliding phasons in moiré ladders, arXiv preprint arXiv:2512.05735 (2025).

- [61] H. Ribeiro, K. Sato, G. Eliel, E. De Souza, C.-C. Lu, P.-W. Chiu, R. Saito, and M. Pimenta, Origin of van hove singularities in twisted bilayer graphene, *Carbon* **90**, 138 (2015).
- [62] Y. A. Bychkov and E. I. Rashba, Oscillatory effects and the magnetic susceptibility of carriers in inversion layers, *Journal of physics C: Solid state physics* **17**, 6039 (1984).